Nonequilibrium interplay between Andreev bound states and Kondo effect

Jiangbo He,[1,2] Dong Pan,[3,4] Guang Yang,[1,2] Mingli Liu,[1,2] Jianghua Ying,[1,2] Zhaozheng Lyu,[1,2] Jie Fan,[1,5] Xiunian Jing,[1,5] Guangtong Liu,[1,2,5] Bo Lu,[6] Dong E. Liu,[7,8] Jianhua Zhao,[3,4,9,*] Li Lu,[1,2,5,9,10,†] and Fanming Qu[1,2,5,10,‡]

[1]*Beijing National Laboratory for Condensed Matter Physics, Institute of Physics, Chinese Academy of Sciences, Beijing 100190, China*
[2]*School of Physical Sciences, University of Chinese Academy of Sciences, Beijing 100049, China*
[3]*State Key Laboratory of Superlattices and Microstructures, Institute of Semiconductors, Chinese Academy of Sciences, Beijing 100083, China*
[4]*College of Materials Science and Opto-Electronic Technology, University of Chinese Academy of Sciences, Beijing 100049, China*
[5]*Songshan Lake Materials Laboratory, Dongguan, Guangdong 523808, China*
[6]*Center for Joint Quantum Studies and Department of Physics, Tianjin University, Tianjin 300072, China*
[7]*State Key Laboratory of Low Dimensional Quantum Physics, Department of Physics, Tsinghua University, Beijing 100084, China*
[8]*Frontier Science Center for Quantum Information, Beijing 100084, China*
[9]*Beijing Academy of Quantum Information Sciences, Beijing 100193, China*
[10]*CAS Center for Excellence in Topological Quantum Computation, University of Chinese Academy of Sciences, Beijing 100190, China*

(Received 22 January 2020; revised 6 July 2020; accepted 29 July 2020; published 17 August 2020)

Andreev bound states (ABSs), as a close resemblance and a prototype of Majorana bound states, attracted particular interest in semiconductor-superconductor hybrids. So far, ABSs were explored as an equilibrium behavior employing tunneling spectroscopy. Under nonequilibrium, theorists did predict that the local density of states (DOS) of the ABSs split and broaden. We investigated an InAsSb quantum dot coupled to two superconductors to explore the nonequilibrium dynamics of ABSs and their interplay with Kondo effect. Through tunneling spectroscopy, we demonstrated a full picture of the nonequilibrium dynamic splitting and broadening of ABSs, which interplays with the nonequilibrium Kondo DOS. Since the observed features might mimic those in the normal superconductor-topological superconductor or Majorana junctions, our discovery could provide a relevant comparison to benchmark the Majorana signal in future experiments.

DOI: 10.1103/PhysRevB.102.075121

I. INTRODUCTION

Hybrid semiconductor-superconductor systems gained tremendous interest recently, due to their prosperity in search of Majorana bound states (MBSs) with which fault-tolerant quantum computation could be implemented [1–7]. In tunneling experiments based on semiconductors with strong spin-orbit coupling (SOC), MBSs manifest as the merging of a pair of Andreev bound states (ABSs) and the appearance of a zero-bias conductance peak (ZBCP) when a magnetic field is applied [1–3,8–11]. ABSs (which in certain cases resemble the Yu-Shiba-Rusinov states [12]), as a close resemblance and a prototype of MBSs, have been investigated to explore the underlying exotic phenomena as well as their similarities and distinctions with the MBSs [13–38]. A quantum dot coupled to two superconducting leads (SC-QD-SC) is one of the prevailing device geometries. In such devices, a superconducting probe was proposed to detect the MBSs sensitively due to the singular superconducting gap edge, though the expected transport behaviors also present analogies with ABSs [36–38]. Experimentally, features of the ABSs including the resonant conductance peaks, the negative differential conductance (NDC) resulting from the convolution of two density of states (DOS) peaks, and replicas of the resonant conductance peaks attributed to a soft induced superconducting gap have been observed [20–28,39]. However, these experiments were performed in the asymmetric coupling regime where an applied bias voltage (V_b) drops mainly on the weakly coupled probe, thus the identified ABSs on the dot is in an equilibrium state with the strongly coupled superconducting lead, i.e., the formation of ABSs is equilibrium. A truly nonequilibrium state can be reached in the symmetric coupling regime where the voltage drops between the dot and both leads. However, in such a regime, the inherently time-dependent high-order (to the infinite) process, multiple Andreev reflection (MAR), dominates the nonlinear subgap features of the current-voltage curves [40,41], usually concealing the observation of the nonequilibrium dynamics of ABSs [41,42]. Consequently, the experiments so far probed either the equilibrium ABSs or the supercurrent and MARs, but not the nonequilibrium spectrum of ABSs [43]. Nevertheless, theoretical works [21,42] did reveal the nonequilibrium dynamics—the splitting and broadening of the ABSs in the sense of local DOS, whose mysterious veil is yet to be uncovered experimentally. Considering the necessity of the application of a voltage in transport experiments, the nonequilibrium manifestations are essential.

Another many-body phenomenon, Kondo effect, plays an important role and competes with the superconductivity in the devices [44–53]. A singlet to doublet (so-called 0-π) ground-state transition of the ABSs has been predicted and

*Corresponding author: jhzhao@semi.ac.cn
†Corresponding author: lilu@iphy.ac.cn
‡Corresponding author: fanmingqu@iphy.ac.cn

demonstrated when $k_B T_K \sim \Delta$ for odd numbers of electrons on the quantum dot [13,23–27,47,54–56], where k_B is the Boltzmann constant, T_K is the Kondo temperature, and Δ is the superconducting gap. The singlet and doublet ground states were further determined explicitly through the examination of the magnetic properties [16]. At the transition point, the two ABSs cross at zero energy, generating a ZBCP or conductance peaks at $V_b = \pm\Delta/e$ using a superconducting probe, which might confuse with the MBSs. Besides, Kondo induced ZBCPs that mimic MBSs were shown to coexist with a superconducting gap when increasing $k_B T_K/\Delta$ through magnetic field (reducing Δ) [22,46]. Moreover, the Kondo DOS anomaly also splits in nonequilibrium [57–59], similar to the predictions for ABSs [21,42]. Given such a complicated situation, a full understanding of the nonequilibrium interplay between the ABSs and the Kondo effect, which might closely resemble the MBSs, is of fundamental importance.

In this work, we investigated SC-QD-SC devices based on InAsSb nanowires to address the nonequilibrium dynamics of the ABSs and their interplay with the Kondo effect. Through electrical gating, the coupling strength between the dot and the two leads can be tuned sequentially to the asymmetric, weak regime (I), the symmetric, intermediate regime (II), and the strong regime (III). In regime I, we observed the 0-π phase transition of the *equilibrium* ABSs resulting from the competition between the superconductivity and the Kondo effect. Importantly, we accessed the truly nonequilibrium condition in the symmetric regime (II) characterized by nearly quantized Kondo conductance peaks. We observed the *nonequilibrium* ABS pairs, the broad replicas as a result of the resonant ABSs and Kondo DOS peaks, and the Kondo enhanced ZBCPs, for odd numbers of electrons. These results demonstrate a full picture of the dynamic splitting and broadening of the ABS DOS in nonequilibrium, as well as the interplay with the nonequilibrium split Kondo DOS. In regime III, MARs and supercurrent were detected, as usually seen for such open quantum dot condition [41,60,61]. Although our measurement is not in the Majorana regime, the observed sharp features from our setup show strong similarities to those in the normal superconductor-topological superconductor or Majorana junctions [36,37] (see Appendix C). Therefore, we believe that our discovery could provide a relevant comparison to benchmark the Majorana signal in the future experiments.

II. DEVICE AND PHYSICAL PICTURES

The ternary compound InAsSb could potentially provide a more promising platform for the research of MBSs, due to the predicted stronger SOC than its binary compounds, InAs and InSb [62,63]. In this work, $InAs_{0.85}Sb_{0.15}$ nanowires were grown on Si (111) substrates by a solid source molecular-beam epitaxy using Ag as seed particles (see Appendix A). After growth, the nanowires were subsequently transferred onto degenerately doped Si substrates covered with 300 nm SiO_2 used for applying a gate voltage (V_G). Two Ti/Al (5/100 nm) contacts separated by ~200 nm were deposited via electron-beam evaporation using standard lithography techniques. Note that an *in situ* soft plasma cleaning of the surface was performed prior to the Ti/Al deposition to improve the interface transparency. Electron transport measurements were carried out employing low-frequency lock-in techniques at ~30 mK in a dilution refrigerator.

Before presenting the experimental results, we describe the physical pictures of the equilibrium and nonequilibrium interplay between the ABSs and the Kondo effect in SC-QD-SC devices identical to ours. Figure 1 illustrates three typical scenarios (one column each) where a single quantum dot level ε_d is asymmetrically [Figs. 1(a)–1(c)] or symmetrically [Figs. 1(d)–1(i)] coupled to two superconducting leads. The symmetric scenarios include either an ideally hard superconducting gap [Figs. 1(d)–1(f)] or a soft gap with finite subgap states [Figs. 1(g)–1(i)]. Here, we restrict to an odd number of electrons on the dot to capture the Kondo effect. In Fig. 1, the thickness of the vertical blue (green) lines indicates the barrier height (voltage drop). For the asymmetric, weak case [Figs. 1(a)–1(c); regime I in our experiment], the coupling between the dot and the right lead is weak but much stronger than that to the left lead, such that a pair of ABSs at energies $\pm\varepsilon$ [sharp red peaks in Figs. 1(a) and 1(b)] form on the dot stemming from the right lead. A voltage V_b drops only at the left barrier, and the left weakly coupled lead works as a tunnel probe. Note that the ABSs are in equilibrium with the mother (right) lead. Figure 1(c) displays the characteristic tunneling spectroscopy for $k_B T_K < \Delta$ at the center of the Kondo ridge, demonstrating resonant differential conductance (dI/dV) peaks (red curves) when the singular gap edge aligns with the ABSs at $V_b = \pm(\Delta + \varepsilon)/e$ and also NDC alongside (blue curves) due to the convolution of the two *sharp* DOS peaks. The turning of the resonant curves at $V_b = \pm\Delta/e$ signifies the crossing of the two ABS branches at $\varepsilon = 0$, i.e., the 0-π transition (as explained later). The conductance features at the crossings of the two ABS branches might mimic the behaviors of MBSs, since they both contribute to zero-bias DOS and thus resonant conductance at $V_b = \pm\Delta/e$ (see Appendix C).

For the symmetric case [Figs. 1(d)–1(i)], to uncover the nonequilibrium dynamics of the ABSs from subgap features of MARs, we consider the intermediate coupling strength such that $k_B T_K > \Delta$, but the high-order MARs are suppressed [42] (regime II in our experiment). Contrary to the asymmetric case, both leads contribute to the formation of the ABSs [Figs. 1(d) and 1(g)]. Moreover, the applied voltage V_b drops equally at the two barriers and renders the nonequilibrium condition for the ABSs where they split into two broadened (also suppressed) pairs, each pinned to the gap of the leads [Figs. 1(e)–1(h)]. Notably, due to the relative shift between the dot level and the chemical potential of the leads, the nonequilibrium ABS energies ε' and ε'' will be slightly different from ε in equilibrium. Figure 1(f) illustrates the spectroscopy including the *broadened*-ABS induced broad resonance peaks (thick red curves) at $\Delta/e < |V_b| < 2\Delta/e$ together with a ZBCP, the supercurrent (red line at $V_b = 0$). Since we assume $k_B T_K > \Delta$ in Fig. 1(f), the ABSs are in the singlet (0) state. In an actual experiment, there can be finite subgap states in the induced superconducting gap [Figs. 1(g)–1(i)], so that a Kondo DOS peak can coexist [Fig. 1(g)] [22,46]. Under nonequilibrium, as shown in Fig. 1(h), the Kondo DOS peak also splits into two peaks, each pinned to the chemical potential of the leads. Compared with the ideal case shown

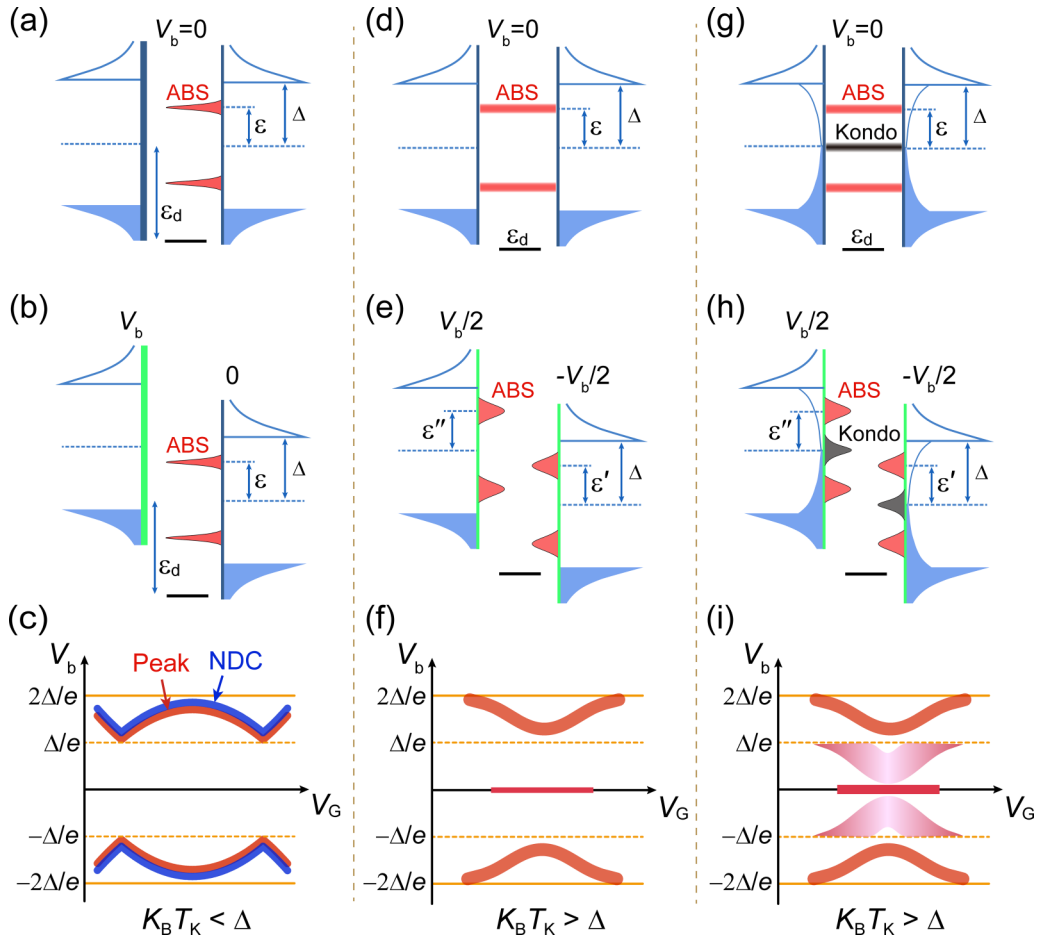

FIG. 1. Illustration of the ABSs and the tunneling spectroscopy. A single quantum dot level ε_d is asymmetrically (a)–(c) or symmetrically (d)–(i) coupled to two superconducting leads. The thickness of the vertical blue (green) lines indicates the barrier height (voltage drop). For the asymmetric case (a)–(c), the left weakly coupled lead works as a tunnel probe, and the ABSs [sharp red peaks in (a) and (b)] stem from and are in equilibrium with the right lead. (c) Characteristic tunneling spectroscopy, demonstrating resonant differential conductance (dI/dV) peaks (red curves) at $V_b = \pm(\Delta + \varepsilon)/e$ and NDC (blue curves). For the symmetric, intermediate-coupling case (d)–(i), both leads contribute to the formation of the ABSs. V_b drops equally at the two barriers and renders the nonequilibrium condition for the ABSs where they split into two broadened pairs, each pinned to the gap of the leads (e),(h). (f) A pair of broad resonance peaks (thick red curves) shows up in the spectroscopy at $\Delta/e < |V_b| < 2\Delta/e$ together with a ZBCP, the supercurrent (red line at $V_b = 0$). For the case with finite subgap states (g)–(i), a Kondo DOS peak emerges (g) and splits into two peaks in nonequilibrium, each pinned to the chemical potential of the leads (h). (i) A Kondo enhanced ZBCP (red line at $V_b = 0$) and a broad replica (pink regions at $|V_b| < \Delta/e$) of the main resonance peaks (thick red curves at $\Delta/e < |V_b| < 2\Delta/e$) are present.

in Fig. 1(f), a broad replica [pink regions at $|V_b| < \Delta/e$ in Fig. 1(i)] of the main resonance peaks (thick red curves at $\Delta/e < |V_b| < 2\Delta/e$) are present when the Kondo peak aligns with the ABSs. In addition, the Kondo DOS also enhances the ZBCP [56,64–67] [red line at $V_b = 0$ in Fig. 1(i)]. More scenarios and an illustration of the similarities between ABSs and MBSs can be found in Appendix C. These physical pictures will be applied to describe our experimental results shown below.

III. EQUILIBRIUM INTERPLAY

We first present the results in the asymmetric, weak-coupling regime (I) in accordance with the scenario of Figs. 1(a)–1(c), where the ABSs and the Kondo correlation are both in equilibrium with the stronger coupled lead. Figure 2(a) shows the differential conductance dI/dV as a function of gate voltage V_G and bias voltage V_b at zero magnetic field, i.e., the superconducting state. For clarity and a better contrast, the V_G range of −9.86 to −9.22 V is divided into two subranges and plotted in different color scales. The horizontal conductance peaks near zero V_b inside the Coulomb diamonds manifest the induced superconducting gap in the nanowire. For diamond α, Kondo resonance peaks can be resolved by killing the superconductivity in the leads using a magnetic field $B = 0.1$ T, as shown in Figs. 2(b)–2(d). Therefore, diamonds α and γ (β) correspond to an odd (even) number of electrons. A Kondo temperature $T_K \approx 0.7$ K is derived at the center of the Kondo ridge in diamond α (see Appendix D), and a coupling asymmetry $\Gamma_1/\Gamma_2 \approx 50$ is extracted from the maximum Kondo conductance $G_{max} = (2e^2/h)4\Gamma_1\Gamma_2/(\Gamma_1 + \Gamma_2)^2$, where h is the Planck constant, Γ_1 and Γ_2 are the coupling strengths between the dot and the two leads. The Kondo peak splits in a magnetic field by $V_b = \pm g\mu_B B/e$, as illustrated by

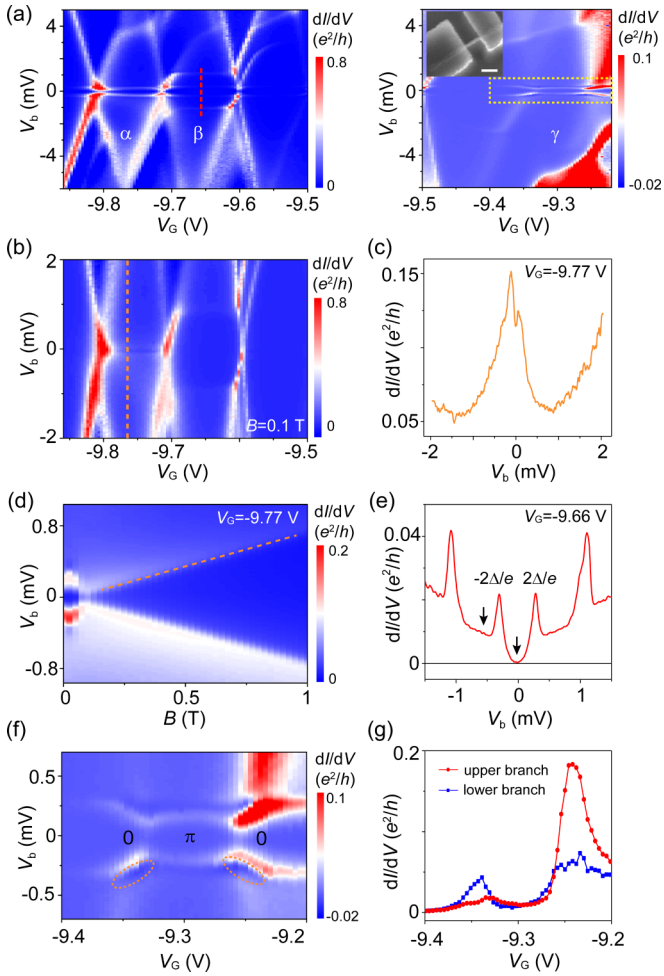

FIG. 2. Equilibrium interplay between the ABSs and the Kondo effect. (a) Differential conductance dI/dV as a function of gate voltage V_G and bias voltage V_b at zero magnetic field. For clarity, the full V_G range of −9.86 to −9.22 V is divided into two subranges and plotted in different color scales. The inset shows the scanning electron microscope image of the device; the scale bar is 200 nm. (b) dI/dV as a function of V_G and V_b measured at $B = 0.1$ T, the normal state. (c) Line cut taken along the orange dashed line in (b) at $V_G = -9.77$ V, showing the Kondo induced ZBCP with Zeeman splitting. (d) dI/dV as a function of B and V_b at $V_G = -9.77$ V, presenting the splitting of the Kondo peak. (e) Line cut taken along the red dashed line in (a) at $V_G = -9.66$ V. The inner and outer peaks correspond to the induced superconducting gap and the excited state, respectively. (f) Zoom-in of the yellow rectangle region in diamond γ in (a). The 0-π phase transition and the NDC (dark blue region, as marked by the two ellipses for the lower branch) can be recognized. (g) Peak conductance for the upper and lower branches of the ABSs resonances shown in (f).

the dashed line in Fig. 2(d), where g is the Landé g factor, μ_B is the Bohr magneton. And $g \approx 12$ can be deduced.

Figure 2(e) shows a line cut along the red dashed line in diamond β in Fig. 2(a). The inner two resonance peaks correspond to the induced gap in the nanowire, $\Delta = 147\ \mu$eV, comparable with bulk Al. Hereafter, the superconducting segments of the nanowire covered by Ti/Al are regarded as the effective leads with the induced gap Δ (see Appendix B). A normal-state to superconducting-state conductance ratio of 24, as indicated by the two black arrows in Fig. 2(e), suggests a relatively hard gap with a small amount of intragap states for the bottom-up fabrication approach [19,54,68]. The outer two peaks result from the inelastic second-order cotunneling process through the ground state and the excited state. A g factor of 12 can again be extracted consistently from the evolution of the cotunneling in a magnetic field (see Appendix E).

Since at the center of the Kondo ridge $k_B T_K < \Delta$, a doublet (π) ground state is expected. Tuning the quantum dot level ε_d to go away from the center ($\varepsilon_d = -U/2$) increases $T_K = \sqrt{U\Gamma/2}\exp[\pi\varepsilon_d(1+\varepsilon_d/U)/2\Gamma]$ (U is the charging energy and Γ is the the total coupling strength) [69] to exceed Δ/k_B and thus a phase transition of the ABSs (crossing of the two branches at $\varepsilon = 0$) will occur, as illustrated in Fig. 1(c). Indeed, such transition was observed for diamonds α (see Appendix G) and γ with an odd number of electrons, as shown in Fig. 2(f), a zoom-in of the yellow rectangle in Fig. 2(a). NDC represented by the dark blue color alongside the resonance peaks, as marked by the two ellipses for the lower branch in Fig. 2(f), was also recognized. Note that replicas were absent within $|V_b| < \Delta/e$, suggesting a relatively hard induced gap with a small amount of intragap states. Another character of the 0-π transition is the abrupt jump of the DOS at the transition point [13,45]. Figure 2(g) displays the peak conductance for the upper and lower branches of the ABSs in Fig. 2(f), showing the fast decay at the 0-π transition points which agrees with theoretical expectations.

IV. NONEQUILIBRIUM INTERPLAY

Next we switch to regime II corresponding to the scenario shown in Figs. 1(g)–1(i), where we show the kernel of this work—the *nonequilibrium* dynamics of the ABSs and their interplay with the Kondo effect. By sweeping V_G towards the positive direction, the coupling strength increases to the intermediate regime. Consequently, Kondo resonances become stronger, as shown in Fig. 3(a) measured at $B = 0.1$ T (normal state). "E" and "O" label the even and odd numbers of electrons, respectively. The nearly quantized Kondo ZBCPs to $2e^2/h$ [black curve in Fig. 3(c)] suggest a symmetric coupling of the two leads [70], a condition required for investigating the nonequilibrium dynamics of the ABSs. In the superconducting state, as displayed in Fig. 3(b), several exotic subgap features arise: (i) Resonances from ABSs under nonequilibrium emerge when $\Delta/e < |V_b| < 2\Delta/e$, as guided by the red dashed lines. Compared to regime I with the 0-π transition, the ABSs here are always in the 0 (singlet) state without crossings, due to the stronger coupling ($k_B T_K \geqslant \Delta$). (ii) Broad replicas of the ABSs resonances are present for $|V_b| < \Delta/e$, as indicated by the green dashed lines. Note that the replicas are absent in the weak-coupling regime, while the replicas here require sizable DOS at the Fermi level. (iii) Compared to the normal state, the zero-bias conductance is enhanced and suppressed for odd and even numbers of electrons, respectively [see the red curve in Fig. 3(c)].

These features can be described in a unified physical picture, as sketched in Figs. 1(g)–1(i). In the symmetric, intermediate coupling ($k_B T_K \geqslant \Delta$) regime (II), for odd numbers

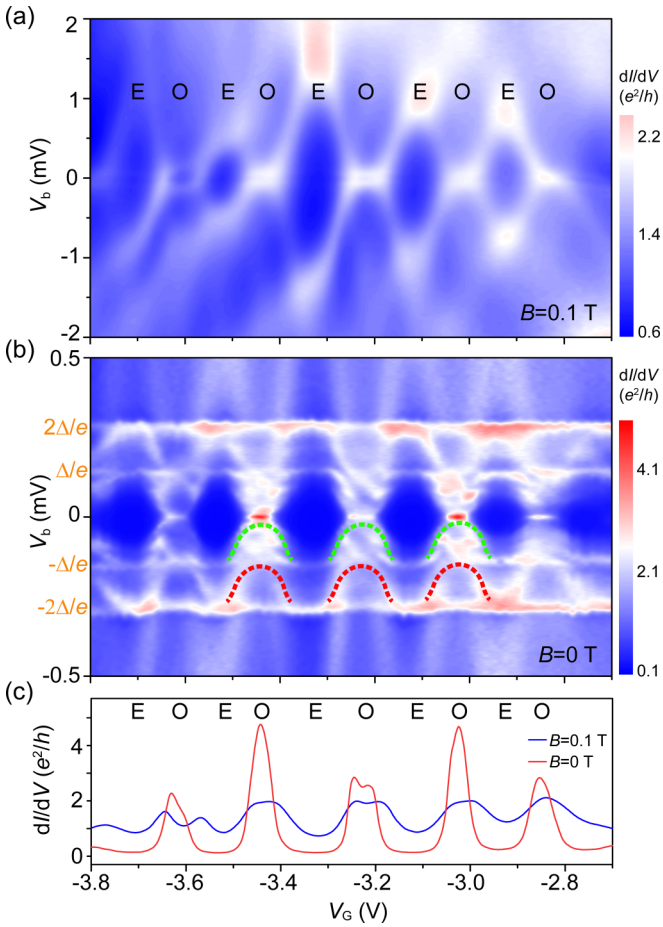

FIG. 3. Nonequilibrium interplay between the ABSs and the Kondo effect. (a),(b) *dI/dV* measured in the symmetric, intermediate-coupling regime (II) at $B = 0.1$ T and 0 T, respectively. The labels E and O mark the even and odd numbers of electrons, respectively. The red dashed lines in (b) highlight the singlet ABSs for $\Delta/e < |V_b| < 2\Delta/e$ and their broad replicas are indicated by the green dashed lines. ZBCPs for odd numbers of electrons can be clearly recognized. (c) Line cuts at $V_b = 0$ for $B = 0.1$ T (blue) and 0 T (red), displaying the Kondo enhanced ZBCPs.

of electrons, ABSs coexist with Kondo DOS on the quantum dot [22,46]. Note that the Kondo DOS shows up in this regime due to the increased coupling strength and intragap states as a result of a higher carrier density [71]. In the weak-coupling regime, the small amount of states at the Fermi level is not sizable enough to generate measurable replicas [22,26,27,39], but here the Kondo DOS appears as a probe (as discussed above) [22]. Consequently, the device fulfills the conditions of Figs. 1(g)–1(i). A good qualitative agreement between the measured spectroscopy shown in Fig. 3(b) and the expected one in Fig. 1(i) is reached, including (i) the resonances of the ABSs for $\Delta/e < |V_b| < 2\Delta/e$, (ii) the broad replicas for $|V_b| < \Delta/e$, and (iii) the Kondo enhanced ZBCPs. Therefore, by realizing the symmetric, intermediate coupling between the quantum dot and the two superconducting leads, we observed the nonequilibrium splitting and broadening of the ABSs and their interplay with the nonequilibrium Kondo DOS. Moreover, the conductance features under nonequilibrium, as

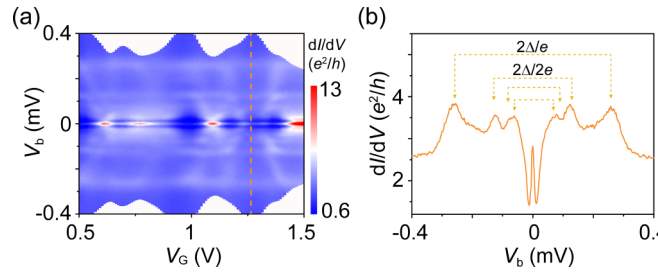

FIG. 4. Supercurrent and MARs in the strong-coupling regime. (a) *dI/dV* as a function of V_G and V_b in the strong-coupling regime (III) measured at $B = 0$ T. (b) Line cut along the dashed line in (a) showing MARs and a sharp ZBCP (supercurrent). The bottom two dashed lines correspond to $2\Delta/3e$ and $2\Delta/4e$, respectively.

shown in Figs. 1(i) and 3(b), might mimic the behaviors of MBSs employing a superconducting probe (see Appendix C).

Notably, NDC alongside the replicas of the equilibrium ABSs was observed in Ref. [27] which leaves an open question that a nontrivial DOS peak at the chemical potential of the superconducting tunnel probe is required. Our findings suggest that the Kondo DOS peak on the dot could shed light on this puzzle.

V. STRONG-COUPLING REGIME

Finally, we present the results in regime III. By sweeping V_G to positive values, the coupling strength is further enhanced, reaching an open quantum dot condition. As shown in Fig. 4(a), continuous ZBCPs were observed, which we attribute to supercurrent [61] (see Appendix I). Accompanied by MARs [Fig. 4(b)], these features are usually detected

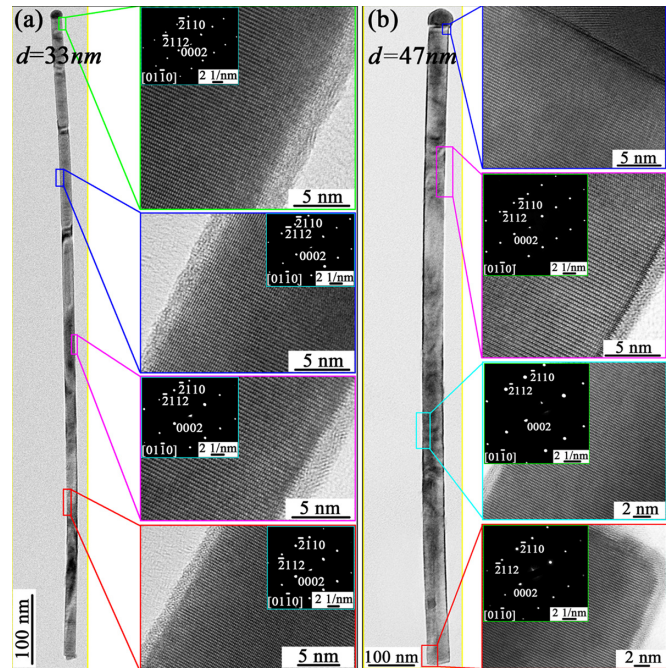

FIG. 5. Characterization of the $InAs_{0.85}Sb_{0.15}$ nanowires. (a),(b) Typical TEM images of $InAs_{0.85}Sb_{0.15}$ nanowires with diameters of 33 and 47 nm, respectively. The insets are selected area electron-diffraction patterns recorded from different areas of the nanowire.

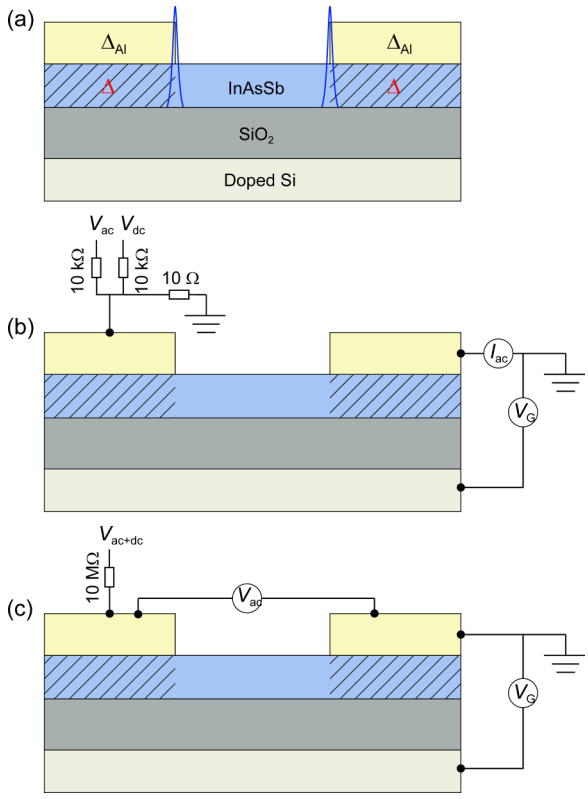

FIG. 6. The device and measurement configurations. (a) Illustration of the InAsSb nanowire (blue shaded) coupled to two Al leads (yellow). The segments (dashed regions) covered by the Al leads are superconducting with an induced gap Δ due to the proximity effect. Tunnel barriers (blue curves) form between the superconducting segments and the middle normal segment, presumably because of band bending resulting from work-function mismatch or doping effect from the contact, as usually observed [26,29,72]. The barrier height, i.e., the coupling strength, can be tuned by a back gate. (b) Two-terminal measurement configuration where a small ac excitation voltage V_{ac} (at 15.7 Hz) and a dc bias voltage V_{dc} were applied ($V_b \approx V_{dc}/1000$) while the ac current I_{ac} was measured. (c) Quasi-four-terminal measurement configuration where a small ac excitation current I_{ac} (at 15.7 Hz) and a dc bias current I_{dc} were applied ($I_{ac} + I_{dc} \approx V_{ac+dc}/10\,\mathrm{M\Omega}$) while the ac voltage V_{ac} was measured. Note that each contact was split into two on the chip.

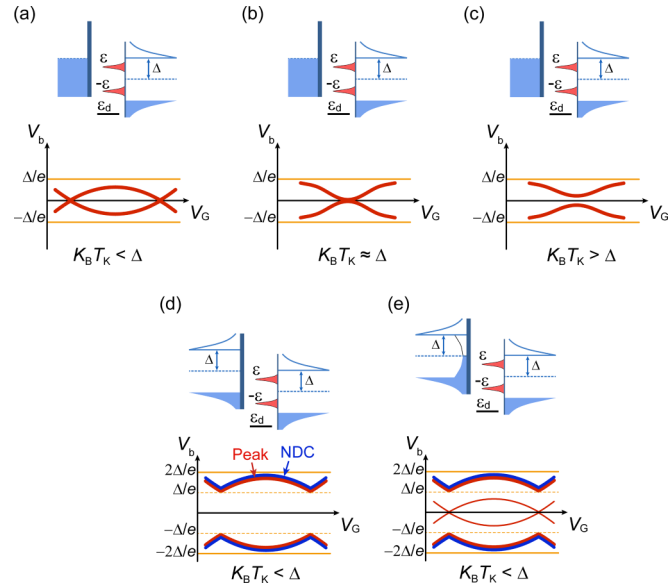

FIG. 7. Illustration of tunneling spectroscopy. (a)–(c) A quantum dot level ε_d is weakly coupled to a normal-metal probe and strongly coupled to a superconductor. A gate voltage V_G controls the level ε_d. In the case of $k_BT_K < \Delta$ at the center of the Kondo ridge (the center of the Coulomb diamond; $\varepsilon_d = -U/2$, where $U \gg \Delta$ is the charging energy) (a), conductance resonances represented by the thick red curves show crosses at zero-bias voltage, i.e., the 0-π transition of the ABSs. When $K_BT_K \approx \Delta$ at the center of the Kondo ridge (b), the two ABS branches cross at the center of the Coulomb diamond. On the other hand, for the case $k_BT_K > \Delta$ (c), the two branches never cross, i.e., always in the singlet state. (d),(e) The quantum dot is weakly coupled to a superconducting lead and strongly coupled to another one. The weakly coupled lead works as a tunnel probe, i.e., carrying the voltage drop. For a superconducting probe with an ideally hard gap (d), the resonances (red curves) appear at $V_b = \pm(\Delta + \varepsilon)/e$ when the gap edge aligns with the ABSs. NDC alongside the resonances (blue curves) will also be present due to the two sharp DOS peaks of the singular gap edge and the ABS. In reality, the induced gap can be soft with sizable single-particle states at the Fermi level (e). In such case, replicas (thin red curves) of the main resonances show up when the Fermi level of the probe aligns with the ABSs. The absence of the replicas in the asymmetric, weak regime in our device suggests that the subgap states are not sizable enough to present measurable features.

in such a strong-coupling regime, without the spectroscopy information of local ABSs [41,60,61,64,67]. In SC-QD-SC devices, as mentioned above, the ABS spectrum including the contribution of Kondo effect was established in the asymmetric-coupling regime, but the ABSs themselves were in equilibrium with the strongly coupled superconducting lead [20–23,26,27]. In this work, the ability of configuring the coupling strength to the symmetric, intermediate regime, where the local subgap states are under nonequilibrium but the high-order MARs are suppressed, enables the observation of the nonequilibrium dynamics of the ABSs and the nonequilibrium interplay with Kondo effect.

VI. SUMMARY

In summary, we studied SC-QD-SC devices based on InAsSb nanowires in three coupling regimes. Importantly, in the symmetric, intermediate regime, we observed behaviors including the ABSs in nonequilibrium, the broad replicas and the Kondo enhanced ZBCPs. These behaviors demonstrate a full picture of the nonequilibrium dynamics of the ABSs and their interplay with the Kondo effect—they split and broaden dynamically. Such picture might also address the puzzles regarding the nontrivial DOS peak [27]. These findings capture the delicate behaviors of the SC-QD-SC devices in both equilibrium and nonequilibrium. The observed conductance features due to ABSs under equilibrium and nonequilibrium show strong similarities to that expected for MBSs in comparable device geometries using a superconducting probe [36,37], and are thus particularly relevant for exploring Majorana physics.

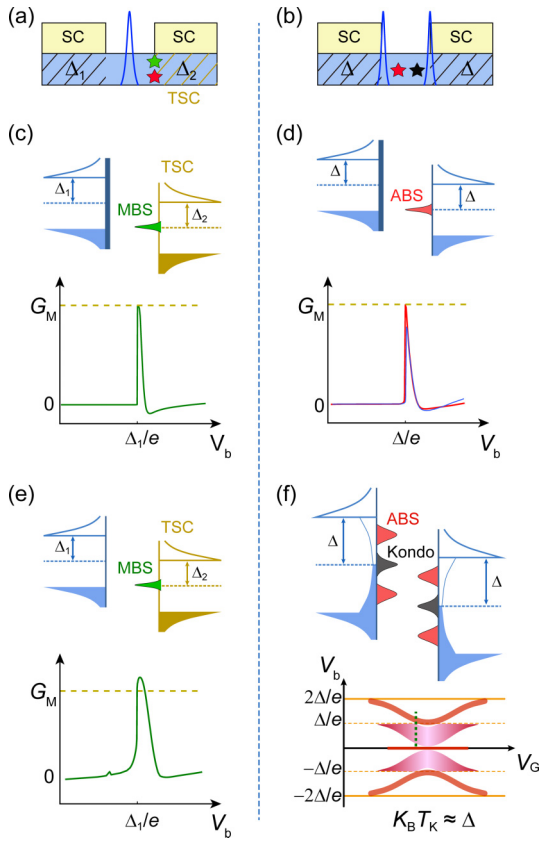

FIG. 8. Illustration of the similarities between MBSs, ABSs, and Kondo DOS. By adjusting the chemical potential of the different segments of the nanowire, the transparency between the superconductor (SC) and the nanowire segments, and the magnetic field, a single barrier (a) or a quantum dot with two barriers (b) can be formed [36–38]. Moreover, topological superconductivity (TSC) with zero-energy MBSs can be induced, as indicated by the green star in (a). Meanwhile, trivial zero-energy ABSs and Kondo DOS can also be present, as marked by the red and black stars, respectively. (c) In the high-barrier limit, the left trivial superconducting segment works as a sensitive probe on the MBS (if present) at the end of the right TSC segment. The differential conductance is suppressed when $|V_b| < \Delta_1/e$, and a jump to a quantized value of $G_M = (4-\pi)2e^2/h$ is expected at $|V_b| = \Delta_1/e$ [36,37]. Such quantization is proposed to be insensitive to temperature broadening, unlike the case with a normal-metal probe. However, if a zero-energy ABS instead of a MBS is present, as indicated by the red star in (a) and (b), the left superconducting segment also probes the ABS at $|V_b| = \Delta_1/e$ in the tunneling limit, as displayed in (d). Although deviation from G_M is common, as represented by the blue curve in the bottom panel in (d), in certain parameter space the differential conductance also shows a sharp upturn to the value of G_M (red curve), very similar as the case of MBS shown in (c) [36]. As displayed in Figs. 1(c), 7(d), and in the measured data Fig. 2(f), the zero-energy ABSs are indeed present, and thus the conductance curve could mimic that of a MBS in some cases. (e) When the barrier height is lower, and thus the transparency increases, the conductance also arises when $|V_b| < \Delta_1/e$ due to contributions of multiple Andreev reflections (bottom panel). Consequently, the conductance can deviate the quantized value G_M. (f) Similar as Figs. 1(h) and 1(i), showing the characteristic spectrum when the ABSs and Kondo DOS coexist. Conductance curves in the bottom panel, e.g., along the green dashed line, can actually mimic the conductance curve shown in (e) for a MBS.

ACKNOWLEDGMENTS

We would like to thank R. Žitko and N. Kang for very fruitful discussions. This work was supported by the National Basic Research Program of China from MOST Grants No. 2017YFA0304700, No. 2016YFA0300601, and No. 2015CB921402, by NSF China Grants No. 11527806, No. 11774405, No. 61974138, and No. 11904257, by Strategic Priority Research Program B of Chinese Academy of Sciences Grants No. XDB28000000 and No. XDB07010100, by Beijing Municipal Science & Technology Commission China Grant No. Z191100007219008, and by Beijing Academy of Quantum Information Sciences Grant No. Y18G08.

J.H. and D.P. contributed equally to this work.

APPENDIX A: GROWTH OF INASSB NANOWIRES

The InAsSb nanowires used in this work were grown on Si (111) substrates by a solid source molecular-beam epitaxy using Ag as seed particles. EDS point analysis of the InAsSb nanowires gives an average atomic ratio of As : Sb = 85 : 15. Figure 5 shows TEM images of $InAs_{0.85}Sb_{0.15}$ nanowires with diameters of 33 and 47 nm, respectively. We can see that the nanowires are high-quality crystals.

APPENDIX B: DEVICE AND MEASUREMENT CONFIGURATIONS

To fabricate the device (see Fig. 6), the InAsSb nanowires were transferred onto degenerately doped Si/SiO_2 (300 nm) substrates with predefined markers using a clean tissue. Afterwards, the nanowires were located by an optical microscope. The patterns of the Ti/Al (5/100 nm) contacts were defined by standard electron-beam lithography techniques followed by electron-beam evaporations. To improve the interface transparency, an *in situ* soft plasma cleaning of the surface was performed prior to the Ti/Al deposition.

The electron transport measurements were performed in a dilution refrigerator at a base temperature of ∼30 mK. Two-terminal or quasi-four-terminal measurement configurations

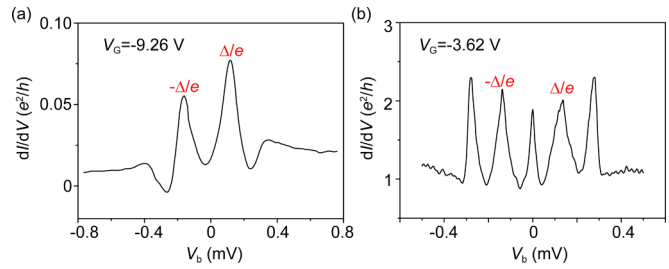

FIG. 9. Line cuts in regimes I and II. (a) Line cut taken from Fig. 2(f) at $V_G = -9.26$ V where the 0-π phase transition occurs, i.e., the two ABSs branches cross at zero energy. (b) Line cut taken from Fig. 3(b) at $V_G = -3.62$ V where nonequilibrium ABSs interplay with Kondo DOS. Both curves show conductance features around $V_b = \pm\Delta/e$, presenting similarities with the nontrivial MBSs as illustrated in Fig. 8.

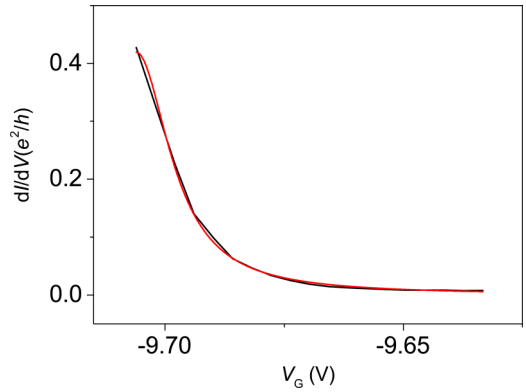

FIG. 10. Fitting (red) of the Coulomb peak (black) at the right side of diamond α in the main text.

were employed depending on the conductance of the device. In the Coulomb blockade regime (Fig. 2), two-terminal measurements were carried out by applying a small low-frequency (15.7 Hz) ac excitation voltage and a dc bias voltage, and the ac current was monitored. When the coupling strength is stronger such that the conductance of the device is high (Figs. 3 and 4), quasi-four-terminal measurements were performed by applying a small ac excitation current (0.1–1 nA) and a dc bias current, and the ac voltage was monitored. For such measurements, the dc voltage was converted through postdata analysis (integral).

APPENDIX C: COMPARISON BETWEEN THE ANDREEV AND MAJORANA BOUND STATES

In this section, we compare the characteristic differential conductance spectroscopy of the ABSs and the MBSs, and show the similarities between them. When a semiconducting nanowire with strong spin-orbit coupling is coupled to two *s*-wave superconductors, such as the SC-InAsSb-SC geometry studied in this work, the zero-energy ABSs, MBSs, and Kondo DOS can be triggered by tuning the chemical potential, the coupling strength, the magnetic field, etc., into a certain parameter space. In principle, the ABSs and the Kondo DOS could mimic the features of the MBSs in the spectroscopy, as we describe below.

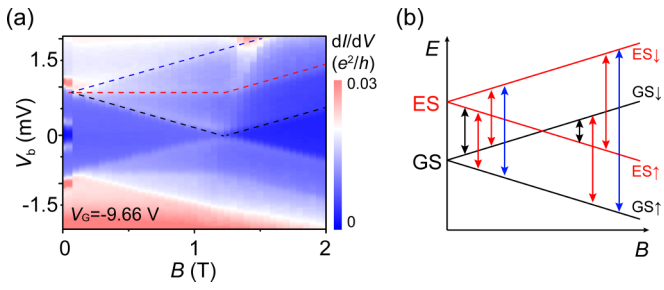

FIG. 11. Transport through the excited states. (a) *dI/dV* as a function of B and V_b at $V_G = -9.66$ V. The dashed lines mark the second-order cotunneling process with the colors in correspondence with the arrows in (b). (b) Zeeman splitting of the ground state (GS) and the excited state (ES). A g factor of 12 can be extracted consistently with the Kondo splitting.

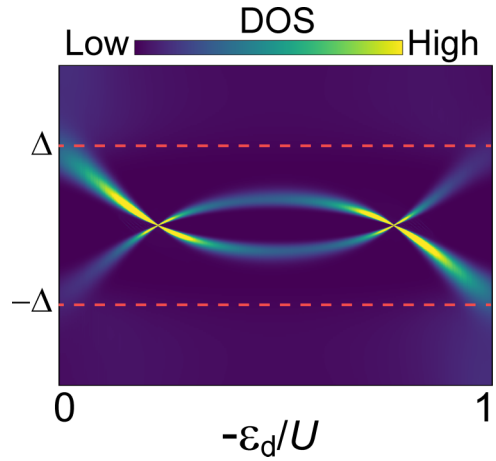

FIG. 12. Calculated ABSs spectrum using a charging energy of $U = 41\Delta$ and a coupling strength of $\Gamma = 4\Delta$, with artificial broadening added to the sharp DOS peaks.

We consider the scenario of a quantum dot formed between the two superconductors, i.e., the case in our work. For the state with an odd number of electrons on the quantum dot, the net spin acts as a magnetic impurity. Consequently, the Kondo correlation coexists and competes with superconductivity. The competition is characterized by the parameter $k_B T_K/\Delta$. When $k_B T_K < \Delta$, the Kondo correlation is suppressed, and the ground state is a doublet (π) state. When tuning the quantum dot level ε_d to go away from the center of the Kondo ridge [see Eq. (2) below], the parameter $k_B T_K/\Delta$ increases to be larger than 1. Therefore, a doublet to singlet phase transition will occur, signified by the crossing of the two ABS branches. Figure 7 illustrates several typical conditions of the conductance spectrum, including some overlaps with Fig. 1. In the case of MBSs, similarities with trivial ABSs could be found in the conductance spectroscopy, as illustrated in Fig. 8 (also see Fig. 9). We can see that in the SC-nanowire-SC devices as we studied, either zero-energy ABSs, MBSs, or Kondo DOS can be generated. In certain parameter settings, they could present similar conductance features in transport measurement.

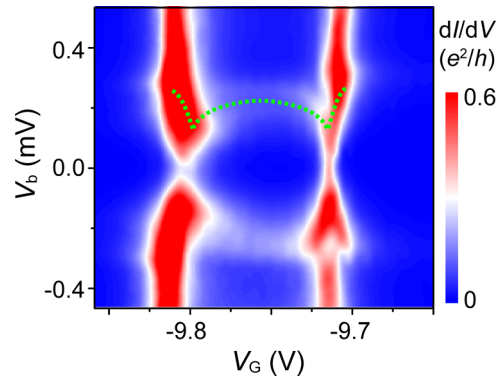

FIG. 13. For diamond α shown in Fig. 2(a), $k_B T_K < \Delta$ at the center of the Kondo ridge, so a 0-π phase transition of the ABSs is expected. As guided by the green dashed line, the resonance peaks follow the characteristics of the 0-π phase transition.

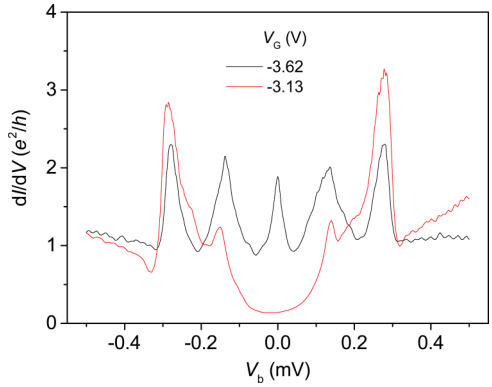

FIG. 14. Line cuts in the symmetric, intermediate-coupling regime taken from Fig. 3(b), for even (red) and odd (black) numbers of electrons on the quantum dot. The conductance is suppressed and enhanced around zero bias for the even and odd states, respectively.

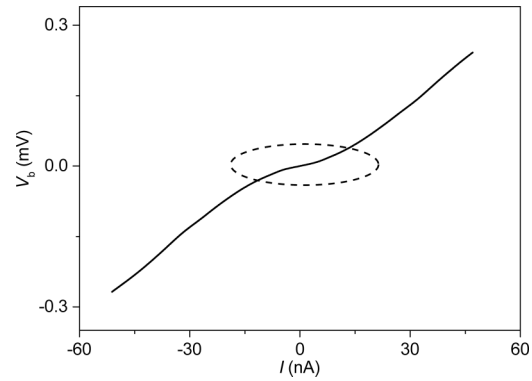

FIG. 15. In the strong-coupling regime, a continuous zero-bias conductance peak which we attribute to supercurrent was observed, as shown in Fig. 4(a). This figure shows a typical current-voltage curve at $V_G = 1.5$ V, illustrating the signature of supercurrent near zero-bias voltage as indicated by the dashed ellipse.

APPENDIX D: EXTRACTION OF THE KONDO TEMPERATURE

Kondo temperature can usually be extracted from the width of the resonant conductance peak. However, in this work, a magnetic field needs to be applied to kill the superconductivity and resolve the Kondo peak, where Zeeman splitting is involved. To deduce the Kondo temperature, we employed the method of Jorgensen *et al.* [26,29]. The normal-state Coulomb peaks in the neighboring even diamond can be expressed in a Lorentzian form

$$G = \frac{e^2}{h}\frac{4\Gamma_1\Gamma_2}{\Gamma^2}\frac{(\tilde{\Gamma}/2)^2}{\varepsilon_d{}^2 + (\tilde{\Gamma}/2)^2}, \tag{1}$$

where $\Gamma = \Gamma_1 + \Gamma_2$, $\tilde{\Gamma} = 1.36\Gamma$, and ε_d is the position of the quantum dot level. Figure 10 shows the fitting (red) of the Coulomb peak (black) at the right side of diamond α. The average coupling strength from the left (not shown) and right Coulomb peaks is $\Gamma = 0.74$ meV. The Kondo temperature T_K can be calculated using (the Boltzmann constant, $K_B = 1$) [69]

$$T_K = \sqrt{U\Gamma/2}\exp[\pi\varepsilon_d(1 + \varepsilon_d/U)/2\Gamma], \tag{2}$$

where $U \approx 6$ meV is the charging energy. At the center of the Kondo ridge, $\varepsilon_d = -U/2$, and $T_K = 0.72$ K.

APPENDIX E: TRANSPORT THROUGH EXCITED STATES

Figure 11 shows the transport features through the excited states. The Zeeman splitting of the ground state (GS) and the excited state (ES) as shown in Fig. 11(b) results in the linear evolution of the conductance peaks, as marked by the dashed lines in Fig. 11(a).

APPENDIX F: CALCULATION OF THE 0-π PHASE TRANSITION

To further confirm the 0-π transition, we solved the single-level Anderson impurity model [73] using the NRG-LJUBLJANA code [74] and calculated the DOS spectrum, as shown in Fig. 12 . A charging energy of $U = 41\Delta$ and a coupling strength of $\Gamma = 4\Delta$ (smaller than that for diamond α since the overall conductance is lower for diamond γ) reproduce the experimental results shown in Fig. 2(f) well.

APPENDIX G: 0-π PHASE TRANSITION IN DIAMOND α

The 0-π phase transition of the ABSs was also observed in diamond α, as shown in Fig. 13. The green dashed line guides the resonance peak.

APPENDIX H: EVEN-ODD EFFECT IN THE INTERMEDIATE REGIME

In the symmetric, intermediate coupling regime (II), an even-odd effect was observed, as shown in Fig. 14. The conductance around zero bias is suppressed and enhanced around zero bias for the even (red curve) and odd (black curve) states, respectively, indicating the contribution of Kondo effect.

APPENDIX I: SUPERCURRENT IN THE STRONG-COUPLING REGIME

In Fig. 4(a), a continuous zero bias conductance peak was observed, which we attribute to supercurrent. By integrating a vertical line-cut, a typical current-voltage curve can be obtained, as shown in Fig. 15. The signature of supercurrent near zero bias voltage can be recognized.

[1] V. Mourik, K. Zuo, S. M. Frolov, S. R. Plissard, E. P. A. M. Bakkers, and L. P. Kouwenhoven, Signatures of majorana fermions in hybrid superconductor-semiconductor nanowire devices, Science **336**, 1003 (2012).

[2] S. M. Albrecht, A. P. Higginbotham, M. Madsen, F. Kuemmeth, T. S. Jespersen, J. Nygård, P. Krogstrup, and C. M. Marcus, Exponential protection of zero modes in majorana islands, Nature (London) **531**, 206 (2016).

[3] H. Zhang, C.-X. Liu, S. Gazibegovic, D. Xu, J. A. Logan, G. Wang, N. van Loo, J. D. S. Bommer, M. W. A. de Moor, D. Car *et al.*, Quantized majorana conductance, Nature (London) **556**, 74 (2018).

[4] F. Wilczek, Majorana returns, Nat. Phys. **5**, 614 (2009).

[5] S. D. Sarma, M. Freedman, and C. Nayak, Majorana zero modes and topological quantum computation, Npj Quantum Inf. **1**, 15001 (2015).

[6] A. Y. Kitaev, Fault-tolerant quantum computation by anyons, Ann. Phys. **303**, 2 (2003).

[7] J. Alicea, Y. Oreg, G. Refael, F. von Oppen, and M. P. A. Fisher, Non-Abelian statistics and topological quantum information processing in 1D wire networks, Nat. Phys. **7**, 412 (2011).

[8] A. Das, Y. Ronen, Y. Most, Y. Oreg, M. Heiblum, and H. Shtrikman, Zero-bias peaks and splitting in an Al-InAs nanowire topological superconductor as a signature of Majorana fermions, Nat. Phys. **8**, 887 (2012).

[9] M. T. Deng, C. L. Yu, G. Y. Huang, M. Larsson, P. Caroff, and H. Q. Xu, Anomalous zero-bias conductance peak in a Nb-InSb nanowire-Nb hybrid device, Nano Lett. **12**, 6414 (2012).

[10] Y. Oreg, G. Refael, and F. von Oppen, Helical Liquids and Majorana Bound States in Quantum Wires, Phys. Rev. Lett. **105**, 177002 (2010).

[11] R. M. Lutchyn, J. D. Sau, and S. Das Sarma, Majorana Fermions and a Topological Phase Transition in Semiconductor-Superconductor Heterostructures, Phys. Rev. Lett. **105**, 077001 (2010).

[12] T. Meng, J. Klinovaja, S. Hoffman, P. Simon, and D. Loss, Superconducting gap renormalization around two magnetic impurities: From shiba to andreev bound states, Phys. Rev. B **92**, 064503 (2015).

[13] R. S. Deacon, Y. Tanaka, A. Oiwa, R. Sakano, K. Yoshida, K. Shibata, K. Hirakawa, and S. Tarucha, Tunneling Spectroscopy of Andreev Energy Levels in a Quantum Dot Coupled to a Superconductor, Phys. Rev. Lett. **104**, 076805 (2010).

[14] T. Dirks, T. L. Hughes, S. Lal, B. Uchoa, Y.-F. Chen, C. Chialvo, P. M. Goldbart, and N. Mason, Transport through Andreev bound states in a graphene quantum dot, Nat. Phys. **7**, 386 (2011).

[15] L. Bretheau, Ç. Ö. Girit, H. Pothier, D. Esteve, and C. Urbina, Exciting Andreev pairs in a superconducting atomic contact, Nature (London) **499**, 312 (2013).

[16] E. J. H. Lee, X. Jiang, M. Houzet, R. Aguado, C. M. Lieber, and S. De Franceschi, Spin-resolved Andreev levels and parity crossings in hybrid superconductor-semiconductor nanostructures, Nat. Nanotechnol. **9**, 79 (2013).

[17] A. P. Higginbotham, S. M. Albrecht, G. Kirsanskas, W. Chang, F. Kuemmeth, P. Krogstrup, T. S. Jespersen, J. Nygard, K. Flensberg, and C. M. Marcus, Parity lifetime of bound states in a proximitized semiconductor nanowire, Nat. Phys. **11**, 1017 (2015).

[18] R. Zitko, J. S. Lim, R. Lopez, and R. Aguado, Shiba states and zero-bias anomalies in the hybrid normal-superconductor Anderson model, Phys. Rev. B **91**, 045441 (2015).

[19] J. Chen, B. D. Woods, P. Yu, M. Hocevar, D. Car, S. R. Plissard, E. P. A. M. Bakkers, T. D. Stanescu, and S. M. Frolov, Ubiquitous Non-Majorana Zero-Bias Conductance Peaks in Nanowire Devices, Phys. Rev. Lett. **123**, 107703 (2019).

[20] J. D. Pillet, C. H. L. Quay, P. Morfin, C. Bena, A. L. Yeyati, and P. Joyez, Andreev bound states in supercurrent-carrying carbon nanotubes revealed, Nat. Phys. **6**, 965 (2010).

[21] B. M. Andersen, K. Flensberg, V. Koerting, and J. Paaske, Nonequilibrium Transport through a Spinful Quantum Dot with Superconducting Leads, Phys. Rev. Lett. **107**, 256802 (2011).

[22] E. J. H. Lee, X. Jiang, R. Aguado, G. Katsaros, C. M. Lieber, and S. De Franceschi, Zero-Bias Anomaly in a Nanowire Quantum Dot Coupled to Superconductors, Phys. Rev. Lett. **109**, 186802 (2012).

[23] B.-K. Kim, Y.-H. Ahn, J.-J. Kim, M.-S. Choi, M.-H. Bae, K. Kang, J. S. Lim, R. López, and N. Kim, Transport Measurement of Andreev Bound States in a Kondo-Correlated Quantum Dot, Phys. Rev. Lett. **110**, 076803 (2013).

[24] W. Chang, V. E. Manucharyan, T. S. Jespersen, J. Nygård, and C. M. Marcus, Tunneling Spectroscopy of Quasiparticle Bound States in a Spinful Josephson Junction, Phys. Rev. Lett. **110**, 217005 (2013).

[25] J. D. Pillet, P. Joyez, R. Žitko, and M. F. Goffman, Tunneling spectroscopy of a single quantum dot coupled to a superconductor: From Kondo ridge to Andreev bound states, Phys. Rev. B **88**, 045101 (2013).

[26] S. Li, N. Kang, P. Caroff, and H. Q. Xu, 0-π; phase transition in hybrid superconductor-InSb nanowire quantum dot devices, Phys. Rev. B **95**, 014515 (2017).

[27] Z. Su, A. Zarassi, J. F. Hsu, P. San-Jose, E. Prada, R. Aguado, E. J. H. Lee, S. Gazibegovic, R. L. M. Op het Veld, D. Car *et al.*, Mirage Andreev Spectra Generated by Mesoscopic Leads in Nanowire Quantum Dots, Phys. Rev. Lett. **121**, 127705 (2018).

[28] L. Tosi, C. Metzger, M. F. Goffman, C. Urbina, H. Pothier, S. Park, A. L. Yeyati, J. Nygård, and P. Krogstrup, Spin-Orbit Splitting of Andreev States Revealed by Microwave Spectroscopy, Phys. Rev. X **9**, 011010 (2019).

[29] H. I. Jørgensen, T. Novotný, K. Grove-Rasmussen, K. Flensberg, and P. E. Lindelof, Critical Current 0$-\pi$ Transition in Designed Josephson Quantum Dot Junctions, Nano Lett. **7**, 2441 (2007).

[30] L. Bretheau, J. I. J. Wang, R. Pisoni, K. Watanabe, T. Taniguchi, and P. Jarillo-Herrero, Tunnelling spectroscopy of Andreev states in graphene, Nat. Phys. **13**, 756 (2017).

[31] J. Gramich, A. Baumgartner, and C. Schönenberger, Andreev bound states probed in three-terminal quantum dots, Phys. Rev. B **96**, 195418 (2017).

[32] J. O. Island, R. Gaudenzi, J. de Bruijckere, E. Burzurí, C. Franco, M. Mas-Torrent, C. Rovira, J. Veciana, T. M. Klapwijk, R. Aguado *et al.*, Proximity-Induced Shiba States in a Molecular Junction, Phys. Rev. Lett. **118**, 117001 (2017).

[33] Z. Su, A. B. Tacla, M. Hocevar, D. Car, S. R. Plissard, E. P. A. M. Bakkers, A. J. Daley, D. Pekker, and S. M. Frolov, Andreev molecules in semiconductor nanowire double quantum dots, Nat. Commun. **8**, 585 (2017).

[34] K. Grove-Rasmussen, G. Steffensen, A. Jellinggaard, M. H. Madsen, R. Žitko, J. Paaske, and J. Nygård, Yu-Shiba-Rusinov screening of spins in double quantum dots, Nat. Commun. **9**, 2376 (2018).

[35] A. Vuik, B. Nijholt, A. Akhmerov, and M. Wimmer, Reproducing topological properties with quasi-Majorana states, SciPost Phys. **7**, 061 (2019).

[36] F. Setiawan, W. S. Cole, J. D. Sau, and S. Das Sarma, Conductance spectroscopy of nontopological-topological

superconductor junctions, Phys. Rev. B **95**, 020501(R) (2017).
[37] Y. Peng, F. Pientka, Y. Vinkler-Aviv, L. I. Glazman, and F. von Oppen, Robust Majorana Conductance Peaks for a Superconducting Lead, Phys. Rev. Lett. **115**, 266804 (2015).
[38] O. A. Awoga, J. Cayao, and A. M. Black-Schaffer, Supercurrent Detection of Topologically Trivial Zero-Energy States in Nanowire Junctions, Phys. Rev. Lett. **123**, 117001 (2019).
[39] A. Kumar, M. Gaim, D. Steininger, A. Levy Yeyati, A. Martín-Rodero, A. K. Hüttel, and C. Strunk, Temperature dependence of Andreev spectra in a superconducting carbon nanotube quantum dot, Phys. Rev. B **89**, 075428 (2014).
[40] A. L. Yeyati, J. C. Cuevas, A. López-Dávalos, and A. Martín-Rodero, Resonant tunneling through a small quantum dot coupled to superconducting leads, Phys. Rev. B **55**, R6137 (1997).
[41] P. Jarillo-Herrero, J. A. van Dam, and L. P. Kouwenhoven, Quantum supercurrent transistors in carbon nanotubes, Nature (London) **439**, 953 (2006).
[42] S. Y. Liu and X. L. Lei, Low-temperature transport through a quantum dot between two superconductor leads, Phys. Rev. B **70**, 205339 (2004).
[43] See Supplemental Material at http://link.aps.org/supplemental/10.1103/PhysRevB.102.075121 for a summary of previous works.
[44] K. J. Franke, G. Schulze, and J. I. Pascual, Competition of Superconducting Phenomena and Kondo screening at the nanoscale, Science **332**, 940 (2011).
[45] J. Bauer, A. Oguri, and A. C. Hewson, Spectral properties of locally correlated electrons in a Bardeen-Cooper-Schrieffer superconductor, J. Phys.: Condens. Matter **19**, 486211 (2007).
[46] T. Domański and A. Donabidowicz, Interplay between particle-hole splitting and the Kondo effect in quantum dots, Phys. Rev. B **78**, 073105 (2008).
[47] T. Meng, S. Florens, and P. Simon, Self-consistent description of Andreev bound states in Josephson quantum dot devices, Phys. Rev. B **79**, 224521 (2009).
[48] A. V. Rozhkov and D. P. Arovas, Josephson Coupling through a Magnetic Impurity, Phys. Rev. Lett. **82**, 2788 (1999).
[49] A. Eichler, R. Deblock, M. Weiss, C. Karrasch, V. Meden, C. Schönenberger, and H. Bouchiat, Tuning the Josephson current in carbon nanotubes with the Kondo effect, Phys. Rev. B **79**, 161407(R) (2009).
[50] T. Sand-Jespersen, J. Paaske, B. M. Andersen, K. Grove-Rasmussen, H. I. Jørgensen, M. Aagesen, C. B. Sørensen, P. E. Lindelof, K. Flensberg, and J. Nygård, Kondo-Enhanced Andreev Tunneling in InAs Nanowire Quantum Dots, Phys. Rev. Lett. **99**, 126603 (2007).
[51] A. Martín-Rodero and A. Levy Yeyati, Josephson and Andreev transport through quantum dots, Adv. Phys. **60**, 899 (2011).
[52] M. Žonda, V. Pokorný, V. Janiš, and T. Novotný, Perturbation theory for an Anderson quantum dot asymmetrically attached to two superconducting leads, Phys. Rev. B **93**, 024523 (2016).
[53] A. Eichler, M. Weiss, S. Oberholzer, C. Schönenberger, A. Levy Yeyati, J. C. Cuevas, and A. Martín-Rodero, Even-Odd Effect in Andreev Transport through a Carbon Nanotube Quantum Dot, Phys. Rev. Lett. **99**, 126602 (2007).
[54] W. Chang, S. M. Albrecht, T. S. Jespersen, F. Kuemmeth, P. Krogstrup, J. Nygard, and C. M. Marcus, Hard gap in epitaxial semiconductor-superconductor nanowires, Nat. Nanotechnol. **10**, 232 (2015).
[55] A. Assouline, C. Feuillet-Palma, A. Zimmers, H. Aubin, M. Aprili, and J.-C. Harmand, Shiba Bound States across the Mobility Edge in Doped InAs Nanowires, Phys. Rev. Lett. **119**, 097701 (2017).
[56] M.-S. Choi, M. Lee, K. Kang, and W. Belzig, Kondo effect and josephson current through a quantum dot between two superconductors, Phys. Rev. B **70**, 020502(R) (2004).
[57] N. S. Wingreen and Y. Meir, Anderson model out of equilibrium: noncrossing-approximation approach to transport through a quantum dot, Phys. Rev. B **49**, 11040 (1994).
[58] Y. Meir, N. S. Wingreen, and P. A. Lee, Low-Temperature Transport through a Quantum Dot: The Anderson Model Out of Equilibrium, Phys. Rev. Lett. **70**, 2601 (1993).
[59] S. M. Cronenwett, T. H. Oosterkamp, and L. P. Kouwenhoven, A tunable kondo effect in quantum dots, Science **281**, 540 (1998).
[60] M. R. Buitelaar, W. Belzig, T. Nussbaumer, B. Babić, C. Bruder, and C. Schönenberger, Multiple Andreev Reflections in a Carbon Nanotube Quantum Dot, Phys. Rev. Lett. **91**, 057005 (2003).
[61] H. I. Jørgensen, K. Grove-Rasmussen, T. Novotný, K. Flensberg, and P. E. Lindelof, Electron Transport in Single-Wall Carbon Nanotube Weak Links in the Fabry-Perot Regime, Phys. Rev. Lett. **96**, 207003 (2006).
[62] G. W. Winkler, Q. Wu, M. Troyer, P. Krogstrup, and A. A. Soluyanov, Topological Phases in $InAs_{1-x}Sb_x$: From Novel Topological Semimetal to Majorana Wire, Phys. Rev. Lett. **117**, 076403 (2016).
[63] J. E. Sestoft, T. Kanne, A. N. Gejl, M. von Soosten, J. S. Yodh, D. Sherman, B. Tarasinski, M. Wimmer, E. Johnson, M. Deng *et al.*, Engineering hybrid epitaxial InAsSb/Al nanowires for stronger topological protection, Phys. Rev. Mater. **2**, 044202 (2018).
[64] M. R. Buitelaar, T. Nussbaumer, and C. Schönenberger, Quantum Dot in the Kondo Regime Coupled to Superconductors, Phys. Rev. Lett. **89**, 256801 (2002).
[65] A. Levy Yeyati, A. Martín-Rodero, and E. Vecino, Nonequilibrium Dynamics of Andreev States in the Kondo Regime, Phys. Rev. Lett. **91**, 266802 (2003).
[66] E. Vecino, M. R. Buitelaar, A. Martín-Rodero, C. Schönenberger, and A. Levy Yeyati, Conductance properties of nanotubes coupled to superconducting leads: signatures of Andreev states dynamics, Solid State Commun. **131**, 625 (2004).
[67] K. Grove-Rasmussen, H. I. Jørgensen, and P. E. Lindelof, Kondo resonance enhanced supercurrent in single wall carbon nanotube Josephson junctions, New J. Phys. **9**, 124 (2007).
[68] Ö. Gül, H. Zhang, F. K. de Vries, J. van Veen, K. Zuo, V. Mourik, S. Conesa-Boj, M. P. Nowak, D. J. van Woerkom, M. Quintero-Pérez *et al.*, Hard Superconducting Gap in InSb Nanowires, Nano Lett. **17**, 2690 (2017).
[69] F. D. M. Haldane, Scaling Theory of the Asymmetric Anderson Model, Phys. Rev. Lett. **40**, 416 (1978).
[70] T. K. Ng and P. A. Lee, On-Site Coulomb Repulsion and Resonant Tunneling, Phys. Rev. Lett. **61**, 1768 (1988).
[71] G. W. Winkler, A. E. Antipov, B. van Heck, A. A. Soluyanov, L. I. Glazman, M. Wimmer, and R. M. Lutchyn, Unified numerical approach to topological semiconductor-superconductor heterostructures, Phys. Rev. B **99**, 245408 (2019).

[72] M. T. Deng, S. Vaitiekėnas, E. B. Hansen, J. Danon, M. Leijnse, K. Flensberg, J. Nygård, P. Krogstrup, and C. M. Marcus, Majorana bound state in a coupled quantum-dot hybrid-nanowire system, Science **354**, 1557 (2016).

[73] P. W. Anderson, Localized magnetic states in metals, Phys. Rev. **124**, 41 (1961).

[74] R. Žitko, NRG LJUBLJANA code for numerical renormalization group calculations, http://nrgljubljana.ijs.si/.